

## CHAPTER 1

### GHOSTBURSTING: THE ROLE OF ACTIVE DENDRITES IN ELECTROSENSORY PROCESSING

Carlo R. Laing

*Institute of Information and Mathematical Sciences,  
Massey University, Private Bag 102-904 NSMC, Auckland, New Zealand  
E-mail: c.r.laing@massey.ac.nz*

Brent Doiron<sup>a</sup>

*Department of Physics, University of Ottawa,  
150 Louis Pasteur, Ottawa, ON, Canada K1N 6N5*

We give an overview of “ghostbursting”, a novel type of bursting observed in sensory processing neurons of weakly electric fish. We discuss the steps taken to understand the bursting mechanism, including experimental manipulations and the development of multi-compartmental and minimal neuron models. Using dynamical systems theory, we emphasise the main differences between this type of bursting and other previous models. We finally review results showing how electrosensory neurons can process different components of dynamic stimuli in parallel with both bursts and isolated spikes.

#### 1. Introduction

Weakly electric fish are nocturnal fresh water animals that thrive in South America and Africa. Over 60 million years they have developed a unique sensory modality — an electrosense. These fish have an electric organ that generates a weak, quasi-sinusoidal electric field. Prey, the fish’s environment, and even communication calls from con-specifics modulate the amplitude of this field. The electrosensory system of the fish detects and processes these modulations to give a neural reconstruction of their environment<sup>1,2</sup>. The ability to use naturalistic dynamic inputs, and the existence of well-

---

<sup>a</sup>Current address: Center for Neural Science, 4 Washington Place, New York, NY 10003.

charted neural feedback pathways and well-characterized single neurons, have recently made weakly electric fish a popular animal in the study of neurocomputational dynamics and processing<sup>3,4</sup>.

Electrosensory inputs are faithfully coded by electroreceptors that densely cover the surface of the animal's body<sup>5</sup>. These receptors project to a dense layer of pyramidal cells in the electrosensory lateral line lobe (ELL) of the fish brain. These cells are the principal output cells within the ELL and they are devoted to the processing of a variety of sensory inputs. The single cell dynamics of these cells exhibit a form of burst discharge termed "ghostbursting"<sup>6,7,8,9</sup>. Bursting behaviour is found in a multitude of sensory cells<sup>4</sup>; however, the ELL and ghostbursting offer distinct advantages for the study of bursting and sensory coding. ELL pyramidal cells are only one synapse from the outside world — an outside world that is simply describable in terms of electric field modulations rather than complex visual or olfactory scenes. Feedback from higher brain centers is segregated and is known to contextually modulate pyramidal cell spiking behaviour<sup>10,11</sup>. Finally, the burst discharge is dependent on active dendritic processes<sup>6</sup> which offers several methods for modulation of burst behaviour<sup>12,13</sup>.

In this chapter we review a host of experimental, computational, and theoretical results of ELL pyramidal cell burst discharge. We first present the core burst mechanism and relate it to experimental and computational results. Next we present several reduced mathematical descriptions of the burst mechanism occurring in ELL pyramidal cells, which are useful for gaining an understanding of the mechanism from the point of view of dynamical systems theory. A comparison between ghostbursting and more classical burst mechanisms will show that ghostbursting has some unique properties. The final section of this review outlines recent results detailing how ELL pyramidal cells use their burst mechanism to differentially code low and high frequency inputs.

## 2. Bursting Mechanism

In the early 1990s, R. W. Turner and L. Maler observed a novel form of burst discharge from ELL pyramidal cells in brain slices of the electric fish *Apteronotus leptorhynchus*<sup>6</sup>. These observations were of a repetitive and high frequency burst discharge in response to a constant current injection; see Fig. 1 for an example recording. The bursts were observed to have a monotonic increase in instantaneous frequency through the burst (i.e. the time between successive action potentials monotonically decreases during

*Ghostbursting: the role of active dendrites in electrosensory processing*

3

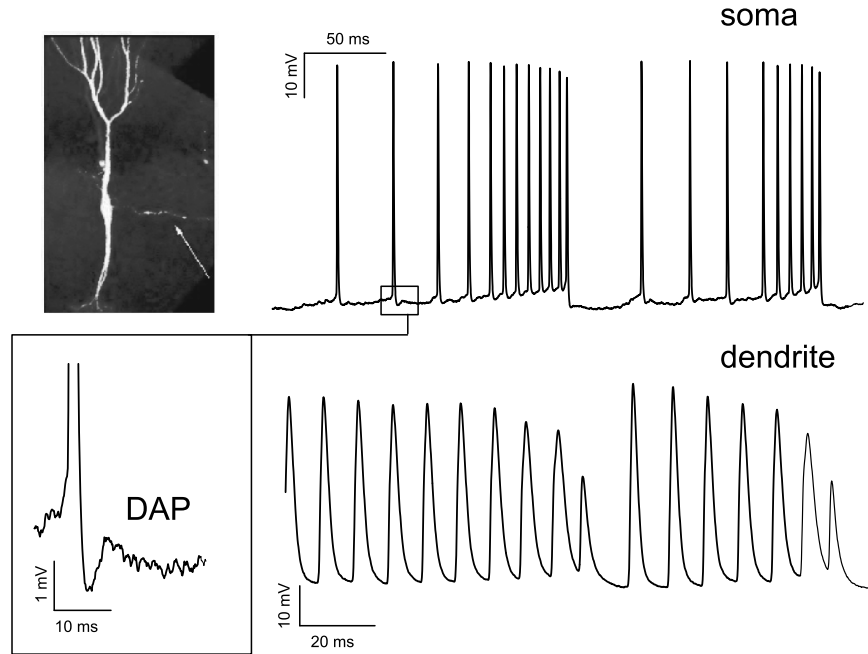


Fig. 1. Ghostbursting in ELL pyramidal cells. Somatic and dendritic membrane potentials recorded from an *in vitro* ELL slice preparation. A constant depolarizing input current was applied to elicit the action potential trains shown in both the somatic and dendritic spike sequences. The expanded portion of the somatic potential shows the depolarizing after-potential (DAP) that occurs shortly after a somatic action potential. The dendritic potential clearly shows the failure of action potential backpropagation after a high frequency somatic spike discharge. This dendritic failure causes a large hyperpolarization at the soma, signalling a burst termination. Note that the somatic and dendritic potentials should not be directly compared since they are recorded from different cells. Data provided by Anne-Marie Oswald. At top left is a confocal image of a Lucifer-yellow filled ELL basilar pyramidal cell.

a burst). This study was also one of the first to determine that there were active sodium channels in the neuron's dendrite, and that their presence was necessary for bursting to occur. Burst mechanisms dependent on active dendritic processes are now quite familiar occurring in varied forms and in diverse systems<sup>4,14</sup>.

Further experimental work<sup>3,9</sup> determined that the acceleration of action potentials (APs) during a burst was due to a gradual broadening of the dendritic APs. Because the somatic APs are narrower than the dendritic, current flows from the dendrite to the soma immediately after the somatic

AP, giving rise to a depolarising after potential (DAP). The broadening of the dendritic APs causes an increase in the size of the DAPs, which results in the acceleration. This acceleration continues until the soma fires two successive APs whose separation in time is less than the refractory period of the dendrite. The dendrite then fails to respond to the second of these APs, the DAP does not appear, and the burst is terminated with a large after-hyperpolarization.

The experimentally-determined aspects of the bursting were successfully modelled by Doiron *et al.*<sup>8</sup>, who constructed and studied a detailed multi-compartmental model of an ELL pyramidal cell. Using measurements and estimates of ion channel densities and parameters, these authors used this model to reproduce realistic APs, different AP refractory periods, and a DAP at the soma. However, it did not reproduce bursting without the introduction of cumulative inactivation of dendritic potassium. The necessity for this assumption will be clear once the ghostburster system is introduced and analysed.

The biophysically-based compartmental model successfully reproduced the bursting seen *in vitro* but, being very detailed, was slow to simulate. Also, it was not clear which aspects of the model were essential for bursting to occur, although it was clear that some components were necessary. Because of this, the authors developed a much simpler model<sup>7</sup>. This simpler model was produced by lumping all of the compartments representing the neuron's dendrite together (there were over 300 compartments representing the dendrite in the model of Doiron *et al.*<sup>8</sup>), and by not including ion channels whose dynamics were not thought to be essential for bursting. The result was a model comprising two compartments (the soma and the dendrite) coupled by a resistance, and described by the following six differential equations:

$$C \frac{dV_s}{dt} = I - g_{Na,s}[m_{\infty,s}(V_s)]^2(1 - n_s)(V_s - V_{Na}) - g_{dr,s}n_s^2(V_s - V_K) - g_L(V_s - V_L) - \frac{g_c}{\kappa}(V_s - V_d) \quad (1)$$

$$\frac{dn_s}{dt} = \frac{n_{\infty,s}(V_s) - n_s}{0.39} \quad (2)$$

$$C \frac{dV_d}{dt} = -g_{Na,d}[m_{\infty,d}(V_d)]^2 h_d(V_d - V_{Na}) - g_{dr,d}n_d^2 p_d(V_d - V_K) - g_L(V_d - V_L) - \frac{g_c}{1 - \kappa}(V_d - V_s) \quad (3)$$

$$\frac{dh_d}{dt} = h_{\infty,d}(V_d) - h_d \quad (4)$$

$$\frac{dn_d}{dt} = \frac{n_{\infty,d}(V_d) - n_d}{0.9} \quad (5)$$

$$\frac{dp_d}{dt} = \frac{p_{\infty,d}(V_d) - p_d}{\tau_p} \quad (6)$$

Subscripts  $s$  and  $d$  refer to somatic and dendritic variables, respectively. Equations (1) and (3) are current balance equations for the soma and dendrite of the neuron, respectively, and the other equations govern the ion channel dynamics. The variables  $m$  and  $h$  are activation and inactivation of  $\text{Na}^+$ , respectively, and  $n$  and  $p$  are activation and inactivation of  $\text{K}^+$ , respectively. Parameter values are  $C = 1\mu\text{F}/\text{cm}^2$ ,  $\tau_p = 5$ ,  $g_{Na,s} = 55$ ,  $V_{Na} = 40$ ,  $g_{dr,s} = 20$ ,  $V_K = -88.5$ ,  $g_L = 0.18$ ,  $V_L = -70$ ,  $g_c = 1$ ,  $\kappa = 0.4$ ,  $g_{Na,d} = 5$ ,  $g_{dr,d} = 15$ , where voltages are measured in mV, time in ms, and conductances in  $\text{mS}/\text{cm}^2$ .  $I$  is the somatic input current,  $g_c$  is the coupling conductance, and  $\kappa$  is the ratio of the somatic area to the total area of the cell. Other functions are  $m_{\infty,s}(V) = 1/[1 + \exp(-(V + 40)/3)]$ ,  $n_{\infty,s}(V) = 1/[1 + \exp(-(V + 40)/3)]$ ,  $m_{\infty,d}(V) = 1/[1 + \exp(-(V + 40)/5)]$ ,  $h_{\infty,d}(V) = 1/[1 + \exp((V + 52)/5)]$ ,  $n_{\infty,d}(V) = 1/[1 + \exp(-(V + 40)/5)]$ ,  $p_{\infty,d}(V) = 1/[1 + \exp((V + 65)/6)]$ . These functions and parameter values are the same as those used in the multi-compartmental model previously discussed<sup>8</sup>. Note that the time constant for  $h_d$  is 1 ms, so  $p_d$  is the slowest variable by a factor of 5.

Behaviour of the ghostburster model (1)-(6) is shown in Fig. 2; for comparative purposes bursts from both experimental data and the large multi-compartmental model are also shown.

We will now describe the bursting in detail, referring to the model (1)-(6) and its behaviour as seen in Fig. 2B. The presence of both sodium and potassium channels in the soma and the dendrite make both capable of

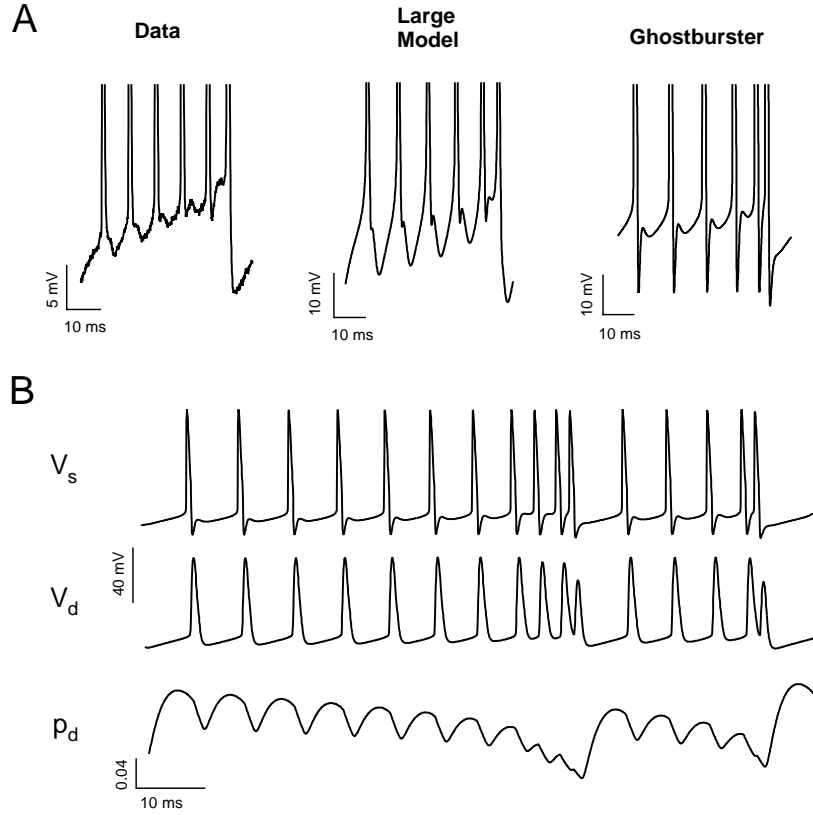


Fig. 2. Ghostbursting in data and models. **A.** Typical somatic bursts in experimentally-observed data (left), the large compartmental model<sup>8</sup> (middle), and the model (1)-(6) for  $I = 9$  (right). The bursts all terminate with a fast “doublet” event. The gradual potentiation of DAPs is visible during the evolution of a burst. **B.** Simulations of (1)-(6) with  $I = 9$ . Top:  $V_s$  (somatic voltage). Middle:  $V_d$  (dendritic voltage). Bottom:  $p_d$  (inactivation of dendritic potassium). Note the rapid reset of  $p_d$  in between bursts.

generating action potentials and somatic DAPs as discussed above. During a burst the variable representing the cumulative inactivation of dendritic potassium,  $p_d$ , slowly decreases. This directly causes the dendritic APs to broaden, as it is associated with the flow of repolarizing potassium ions. This causes the DAPs to slowly grow in magnitude, which in turn accelerates the rate of production of APs in the soma. This acceleration occurs

until the soma fires two APs (a “doublet”) that are so close together that the dendrite can respond to only the first of this pair, as the second occurs within the refractory period of the dendrite. This failure of the dendrite to respond to the second AP in the doublet (seen as a drop in AP amplitude in the middle panel of Fig. 2B) eliminates the current that would normally flow from the dendrite to the soma, and thus the DAP. There is then a relatively long wait until the soma fires again, of its own accord. During this gap (the “inter-burst interval”)  $p_d$  recovers to its value near the start of a burst and the process starts again. While there is no direct experimental evidence for a  $p_d$ -like variable in ELL pyramidal cells, it was included in the models as the most plausible mechanism for causing the slowly broadening dendritic APs during a burst. Frequency-dependent spike broadening resulting from potassium inactivation has been shown in several invertebrate systems<sup>15,16</sup>.

Now that a reduced two-compartment description of ELL pyramidal cell behaviour is available, a more mathematical understanding of ELL burst discharge is possible. This will allow for a better comparison between ghostbursting and other more traditional types of bursting. This is the focus of the next section.

### 3. Ghostburster Dynamics

A bifurcation analysis of the full system (1)-(6) using the injected current  $I$  as a parameter was presented in Doiron *et al.*<sup>7</sup>, and a similar diagram is shown in Fig. 3. For small enough  $I$ , the system is quiescent. As  $I$  is increased, there is a saddle-node bifurcation of fixed points on an invariant circle, leading to periodic firing. This bifurcation is seen in a number of other model neurons<sup>17,18</sup>. As the current is increased further, there is a saddle-node bifurcation of limit cycles, and the system starts bursting. The bifurcation diagram suggests that for some values of  $I$ , this bursting is *chaotic*<sup>19</sup>. This chaotic nature was shown by Doiron *et al.*<sup>7</sup>, where the most positive Lyapunov exponent of (1)-(6) was calculated as a function of  $I$ . Intervals of  $I$  for which this exponent was positive were found, indicating that the dynamics were chaotic. Note that the chaotic nature implies that no two bursts will be identical. This is clearly seen in Fig. 2B.

A standard way of analysing bursting systems<sup>18,20,21</sup> is to notice that for many of them there is a separation of timescales, so that the system can

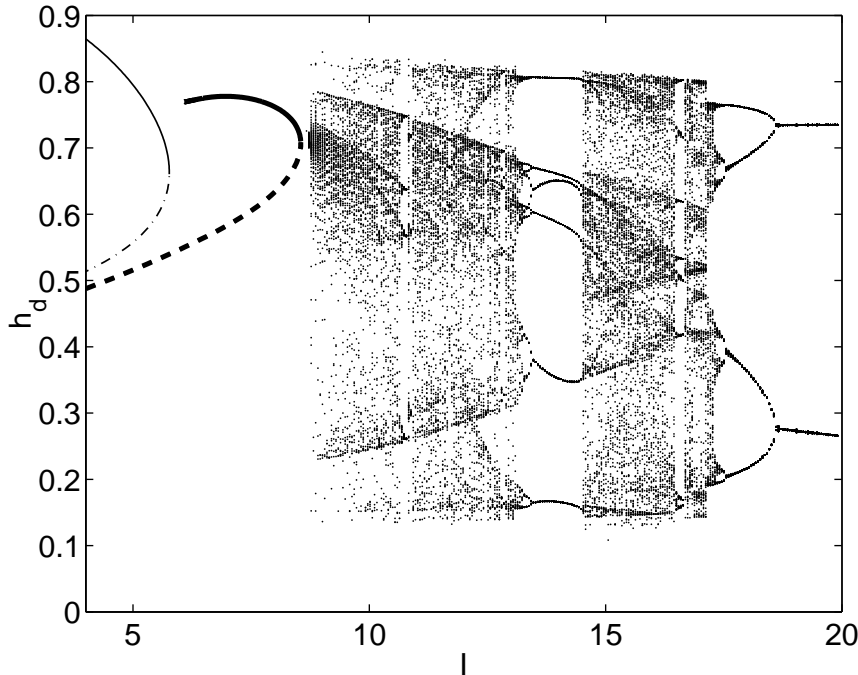


Fig. 3. Bifurcation diagram for (1)-(6) as a function of  $I$ . The value of  $h_d$  for the stable and unstable fixed points is shown with the thin solid and dash-dotted lines, respectively. The maximum of  $h_d$  over one period for the stable and unstable periodic orbits is shown by the thick solid and dashed lines, respectively. During bursting, the maximum values of  $h_d$  during a period of 500 ms are shown (after transients).

be written

$$\frac{dx}{dt} = f(x, y) \quad (7)$$

$$\tau \frac{dy}{dt} = g(x, y) \quad (8)$$

where  $1 \ll \tau$  and  $f$  and  $g$  are of similar magnitude. The analysis proceeds by treating  $y$  in (7) as a constant, and performing a bifurcation analysis of the “fast” subsystem (7) with  $y$  as the bifurcation parameter, yielding, typically, bistability between a periodic oscillation in  $x$  and a stable steady state, over a range of values of  $y$ . Now considering the full system (7)-(8), imagine that  $g(x, y)$  is such that when  $x$  is oscillating,  $y$  slowly increases (say) until it reaches a value for which there is a bifurcation destroying

the periodic oscillation (for example, a homoclinic bifurcation). The system then jumps to the branch of fixed points, on which  $y$  slowly decreases (say). This continues until another bifurcation destroys the fixed point (for example, a saddle-node bifurcation of fixed points), at which point the system jumps back to the branch of periodic oscillations, and the cycle starts again. Thus the system as a whole slowly alternates between periodic firing and quiescence, i.e. it bursts<sup>18</sup>.

Another possibility is that the fast subsystem (7) is not bistable for any value of  $y$ , but does have bifurcations of fixed points and periodic orbits. If  $y$  is at least two-dimensional,  $y$  could undergo slow oscillations that cause (7) to repeatedly cycle through regions in which there were alternately oscillations and fixed points, thus giving bursts of oscillations separated by quiescent periods<sup>18</sup>. By understanding the bifurcations that (7) undergoes as  $y$  is varied, qualitative aspects of the bursting can be determined. Indeed, by combining pairs of bifurcations in different ways, a large number of theoretically-possible bursters can be enumerated<sup>20</sup>.

This type of analysis was also carried out for the system (1)-(6), even though the separation of timescales is not so clear, with  $p_d$  being the slowest variable by a factor of only 5 (see Eq. (6)). Treating  $p_d$  as a parameter, the “fast” subsystem (1)-(5) undergoes a bifurcation from periodic firing with one oscillation of  $V_d$  per period to periodic firing with two oscillations of  $V_d$  per period as  $p_d$  is decreased, as shown in Fig. 4. The top panel in this Figure provides a “skeleton” upon which the bursting of the full system can be superimposed.

To determine the dynamics on this skeleton, we need to know the dynamics of  $p_d$ . From (6) we see that  $p_d$  is driven by  $V_d$  only, and so the  $p_d$  nullcline (where  $dp_d/dt = 0$ ) will be a curve in the  $p_d - V_d$  plane. This is plotted in Fig. 5, along with the curves from the top panel of Fig. 4 and a single burst of the full system (1)-(6). We see that during the first part of the burst,  $p_d$  slowly decreases — this is due to the trajectory spending most of its time in the region where  $dp_d/dt < 0$ . The burst ends when  $p_d$  decreases below the value at which there is a bifurcation in the fast subsystem ( $p_d \approx 0.102$ ), a fast “doublet” is fired, and  $V_d$  drops below the  $p_d$  nullcline.  $p_d$  is then reinjected to higher values, crosses the nullcline again, and another burst starts.

Finally, by choosing parameter values carefully it is possible to use the two saddle-node bifurcations shown in Fig. 3 to set the timescales of bursting. This effect is shown in Fig. 6 where the slow passage associated with both the saddle-node bifurcations of fixed points and limit cycles dictate

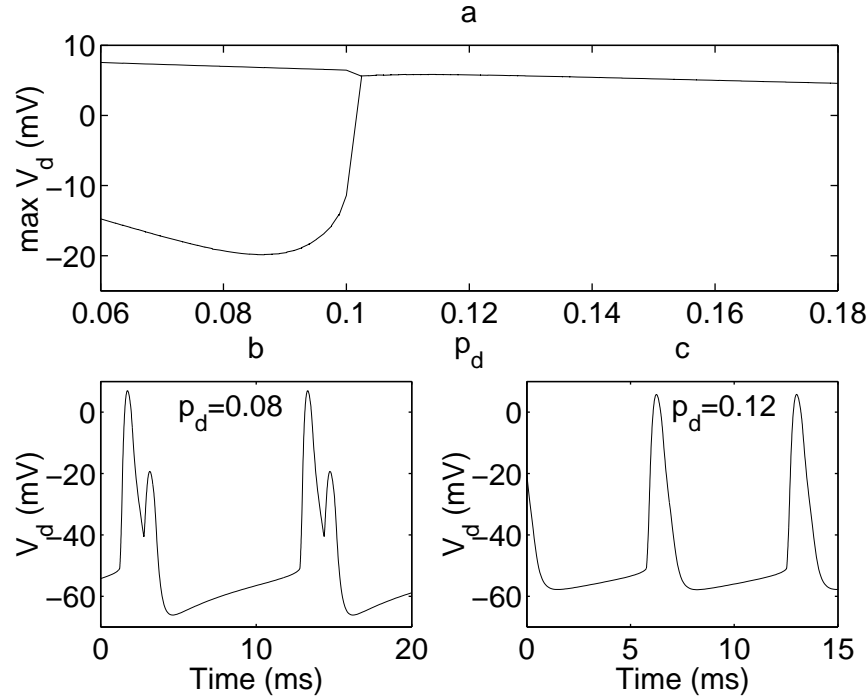


Fig. 4. Bifurcation analysis of the fast subsystem (1)-(5) for  $I = 9$ . There is a bifurcation from period-one firing to period-two firing as  $p_d$  is decreased. a: Maxima of  $V_d$  during periodic firing as a function of  $p_d$ . b:  $V_d$  as a function of time for  $p_d = 0.08$ . c:  $V_d$  as a function of time for  $p_d = 0.12$ .

the inter-burst and burst timescales respectively. The slow passage through a region of phase space where a saddle-node bifurcation occurs is often referred to as sensing the ghost of the bifurcation<sup>22</sup>; it is this effect that gives the bursting mechanism its name. (Also, the common name for the weakly electric fish *Apteronotus leptorhynchus* is the “brown ghost knife fish”.)

#### 4. Unique Features

In this section we contrast the ghostbuster with other models of bursting, pointing out some unique features. As mentioned in Sec. 2, many bursting systems are analysed by splitting them into “fast” and “slow” subsystems<sup>18,20</sup>. For many of these systems, the fast subsystem is bistable for some values of the (one-dimensional) slow variable (for example, the

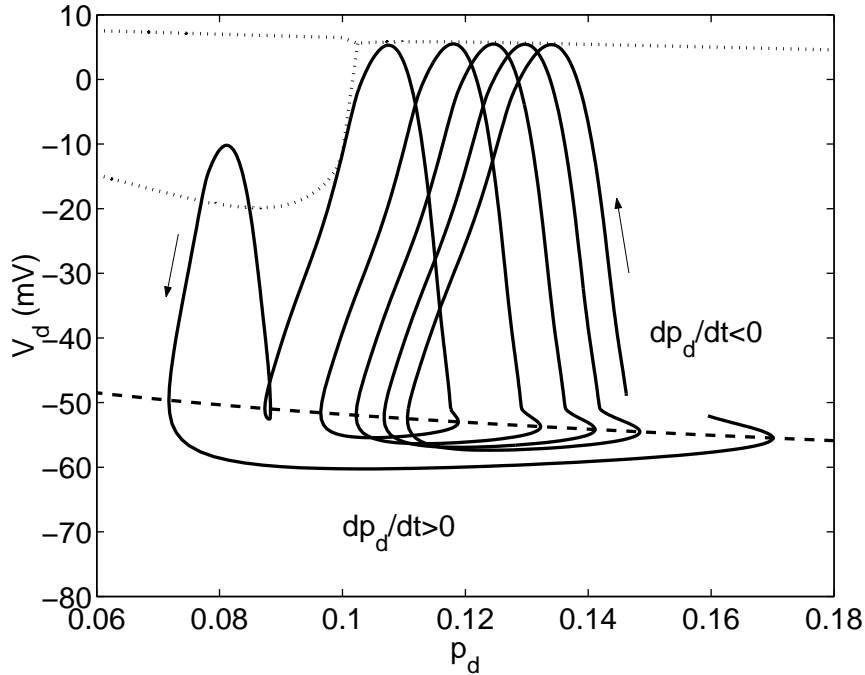


Fig. 5. A single burst (solid line) superimposed on the skeleton shown in the top panel of Fig. 4 (dotted). The  $p_d$  nullcline is shown dashed (above this,  $dp_d/dt < 0$ , and below it  $dp_d/dt > 0$ ). Arrows show the direction through the burst.

square-wave or elliptic bursters<sup>18,21</sup>). Upon splitting the model (1)-(6) like this, with  $p_d$  as the slow variable, we do not find bistability for any value of  $p_d$ . Indeed, we do not even find stable fixed points for any relevant value of  $p_d$ , only a family of periodic orbits. In contrast, some other bursting models do not have bistability in their fast subsystem, but have a slow subspace with two or more dimensions (for example, the parabolic burster<sup>18,21</sup>). The ghostburster is not of this type either, as we have only one slow variable,  $p_d$ .

Another difference between the ghostburster and any other bursters of which we are aware is the presence of a period-one to period-two bifurcation in the fast subsystem (see Fig. 4). This transition involves a rapid change in the appearance of the periodic orbit over a small interval of  $p_d$  values, and is a result of the threshold nature of action potential (AP) production. To the right of the bifurcation in Fig. 4, the DAP that appears at the soma is not large enough to trigger another AP, but to the left it is, resulting

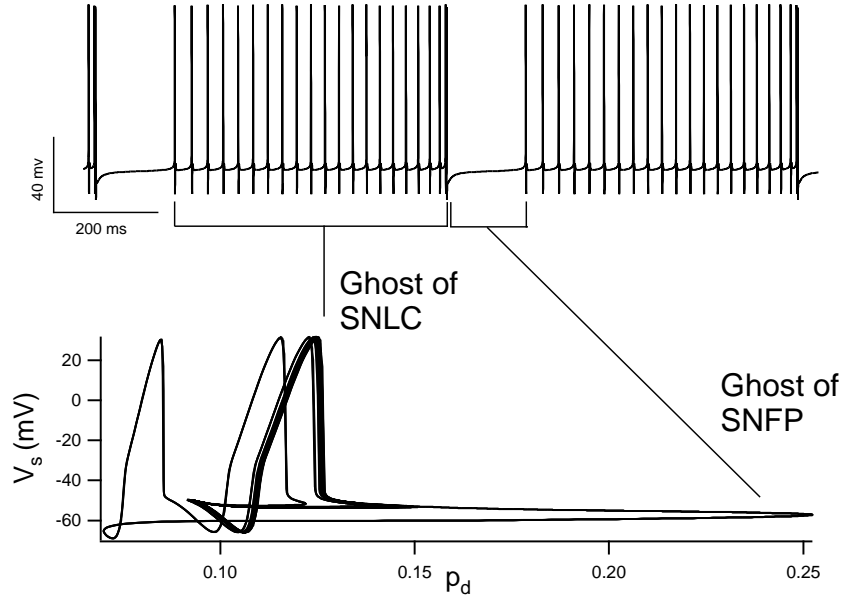


Fig. 6. A demonstration of the effects of the saddle-node bifurcations on the dynamics. Simulations of the system (1)-(6) with  $I = 5.748$  and  $g_{D,r,d} = 12.14$ . These values put the system near both the saddle-node bifurcation of fixed points (SNFP) and of limit cycles (SNLC) shown in Fig. 3. Top: Time series of  $V_s$ ; note the clear bursting pattern. Bottom: Phase trajectory as projected in the  $(V_s, p_d)$  axis. In phase space the burst discharge occurs with the slow passage through the ghost of the SNLC, where the firing is almost periodic. The inter-burst interval is determined by another slow passage, this time through the ghost of the SNFP.

in two APs in quick succession. It is this “doublet”, and the failure of the dendrite to respond to the second of the APs, that allows  $p_d$  to recover and another burst to commence. The exact nature of this bifurcation has not been determined, but it may be related to the formation of a canard<sup>23</sup>.

A further difference is in the way the system responds when the slowest timescale in the system,  $\tau_p$ , is increased. For other bursters such as the square-wave, parabolic and elliptic<sup>18</sup>, increasing the timescale of the slow process(es) leads to the durations of both the active (spiking) and quiescent phases of the bursting being increased. This continues as the slow timescale is made arbitrarily large. However, for the ghostbuster there are qualitative changes as  $\tau_p$  is increased. As this timescale is increased, recognisable bursts become longer, but the interburst intervals do not. Instead, between bursts

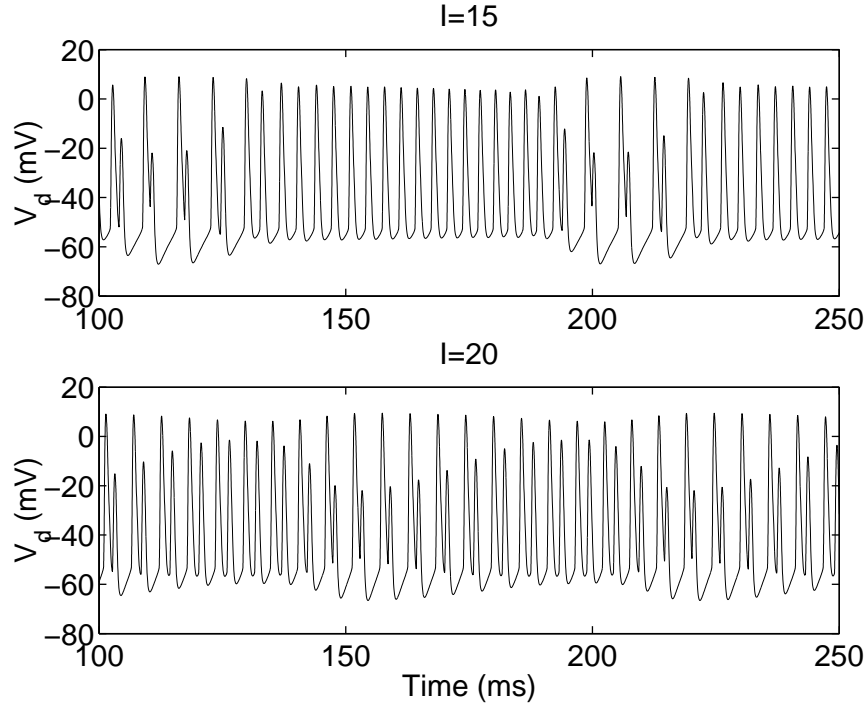


Fig. 7. The effects of increasing the slowest timescale,  $\tau_p$ .  $V_d$  as a function of time for  $\tau_p = 55\text{ ms}$  and  $I = 15$  (top) and  $I = 20$  (bottom).

there are a number of doublets that occur as  $p_d$  slowly increases to its value at the start of the burst, as shown in Fig. 7 (top). This is because the interburst interval is not actually caused by the fast subsystem tracking a branch of stable fixed points, as happens in many other bursters<sup>20</sup>. Fig. 7, bottom, shows the effect of further increasing  $I$  on the behaviour shown in the top panel; we have a slow modulation of doublets, with dendritic failure to a greater or lesser extent. Decreasing  $I$  leads to periodic firing, while increasing  $\tau_p$  further just increases the number of doublets between bursts (not shown). There is also a lower limit on the value of  $\tau_p$  (approximately 2 ms), below which the system does not burst for any values of  $I$  (data not shown). Thus,  $\tau_p$  must lie in a finite interval for ghostbursting to occur.

It is for these reasons that ghostbursting can be regarded as “novel”.

## 5. Extensions and Other Work

Various aspects of the ghostbursting described above have been investigated further<sup>13,24,25,26,27,28</sup>. We now describe some of this work in more detail.

### 5.1. Reduced Models

Soon after the model (1)-(6) had been investigated, Laing and Longtin<sup>27</sup> presented a minimal model of a neuron that showed ghostbursting, in the sense of producing qualitatively correct bursts, and showing the appropriate transitions as the injected current was changed. This model was a modified integrate-and-fire neuron, with a second variable to cluster the action potentials. The equations are

$$\frac{dV}{dt} = I - V + c \sum_n H(t_n - t_{n-1} - r) \delta(t - t_n - \sigma) \quad (9)$$

$$\frac{dc}{dt} = -c/\tau + (B + Cc^2) \sum_n \delta(t - t_n) \quad (10)$$

with the rule  $V(t_n^+) = 0$  if  $V(t_n^-) = 1$ , where  $H(\cdot)$  is the Heaviside step function,  $\delta$  is the Dirac delta function,  $I$  is the injected current, and  $r, \sigma, \tau, B$  and  $C$  are constants. The  $t_n$  are the firing times,  $r$  corresponds to the dendritic refractory period and  $\sigma$  mimics the effective delay between a somatic action potential and the appearance of a DAP caused by current flow from the dendrite to the soma.

Typical bursting behaviour of the model (9)-(10) is shown in Fig. 8. We see that  $c$  is incremented at each action potential:  $c \mapsto c + B + Cc^2$ , and decays exponentially to zero otherwise, with a time constant  $\tau$ . Also, at a fixed delay ( $\sigma$ ) after most action potentials,  $V$  is incremented by the current value of  $c$ . If two successive action potentials are too close in time (less than  $r$  apart),  $V$  does not get incremented after the second of those two APs, and there is a gap until the next burst starts. If  $I$  is gradually decreased, the bursts get longer, and then the system starts behaving periodically, in agreement with the other models (not shown).

Because (9)-(10) is piecewise linear, we can explicitly integrate from one

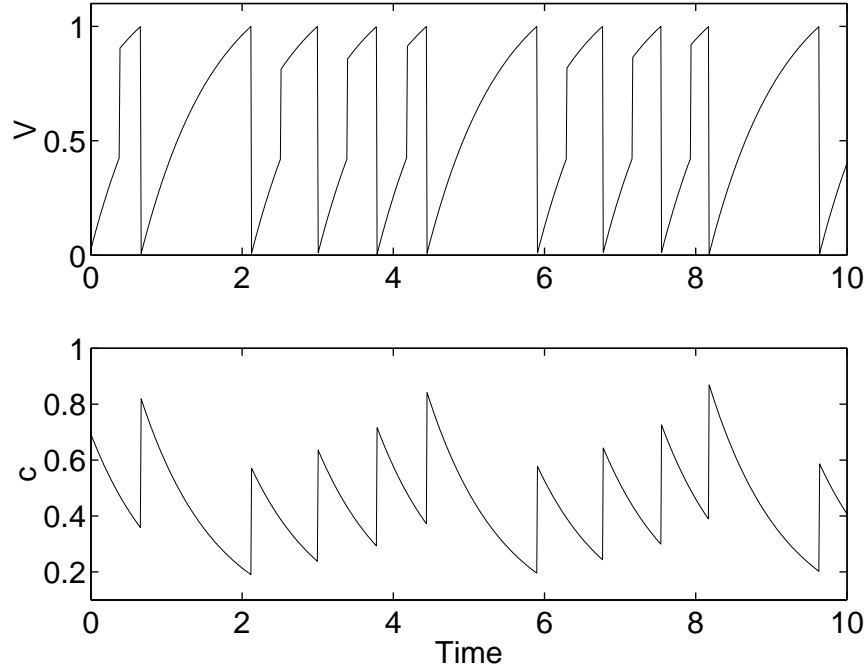


Fig. 8. Voltage ( $V$ , top) and  $c$  (bottom) as functions of time for the minimal model (9)-(10). Two complete bursts are shown. Parameter values are  $\sigma = 0.4$ ,  $\tau = 1$ ,  $r = 0.7$ ,  $B = 0.35$ ,  $C = 0.9$ ,  $I = 1.3$ .

firing time to the next, obtaining a firing time map

$$\Delta_{n+1} = \begin{cases} \sigma & \text{if } \Delta_n > r \text{ and } I + s_n > 1 \\ \sigma + \ln[s_n/(1-I)] & \text{if } \Delta_n > r \text{ and } I + s_n < 1 \\ \ln[I/(I-1)] & \text{if } \Delta_n < r \end{cases} \quad (11)$$

$$c_{n+1} = c_n e^{-\Delta_{n+1}/\tau} + B + C \left[ c_n e^{-\Delta_{n+1}/\tau} \right]^2 \quad (12)$$

where  $\Delta_n = t_n - t_{n-1}$ ,  $c_n = c(t_n^+)$ , and  $s_n = c_n e^{-\sigma/\tau} - I e^{-\sigma}$ .

This exact map avoids the introduction of errors through numerical integration and allows one to quickly generate a sequence of firing times. It is also easy to use this map to see how changing parameters will change the behaviour of the system (9)-(10) through, for example, bifurcations of specific types of solution<sup>27</sup>. Although bursting in maps has been previously studied<sup>29</sup>, we believe this to be the first map from one firing time to the next that shows bursting.

### 5.2. Periodic Forcing

The pyramidal cell under study receives input from electroreceptors on the skin of the fish<sup>5</sup>. These detect the electric field around the fish. For a freely-swimming animal, the electric field and thus the input to the pyramidal cells will be time-dependent. A natural way to study the effects of time-dependent input on a pyramidal cell is to study periodic input. This periodic input could come from at least two sources: the periodic electric organ discharge itself, or the “beat” frequency that occurs when two fish with different frequencies meet.

Laing and Longtin<sup>27</sup> studied the minimal model (9)-(10) with sinusoidal modulation of the input current  $I$ . Because of the simplicity of the system, a map for firing times could again be derived. These authors used this map to show how resonance (Arnol'd) tongues — in which the neuron is “mode locked” to the forcing frequency — could be traced out in parameter space. They also investigated the effects of noise on such a map and showed that the model neuron could display *stochastic resonance*<sup>30</sup>, in which the signal-to-noise ratio is maximised at a moderate value of noise intensity, provided that bursts were used as the “signal”, rather than all action potentials. Subsequently, Laing and Coombes<sup>24</sup> studied the model (9)-(10) under arbitrary periodic forcing, analysing general  $p : q$  mode locking, for which the neuron fires  $p$  times during  $q$  forcing periods. They studied the stability of these types of solutions by linearising about them, and found non-smooth bifurcations in the flow that had been previously overlooked.

Laing and Longtin<sup>28</sup> also studied the model (1)-(6) under sinusoidal modulation of the input current  $I$ . They found that the modulation could shift the value of  $I$  corresponding to the periodic/burst transition (see Fig. 3) in either direction, depending on the frequency of modulation. They also found stochastic resonance, provided that bursts be used as the signal rather than action potentials, in agreement with previous results<sup>27</sup>.

### 5.3. Burst Excitability

The concept of “burst excitability” was first introduced by Laing and Longtin<sup>27</sup> and then studied in detail by Laing *et al.*<sup>26</sup> Burst excitability is a generalisation of “normal” excitability, seen in neural and other systems<sup>18,21</sup>. The usual notion of excitability is that a system is at rest and there exists a threshold such that if a perturbation pushes the system past the threshold, it undergoes a large stereotypical excursion in phase space before returning to rest. If the perturbation is not large enough to push the

system past threshold, it returns directly to the rest state.

Such excitability occurs in neural systems for which the bifurcation from quiescence to periodic firing as the injected current is increased is a saddle-node-on-a-circle bifurcation<sup>17</sup>. The essential ingredients here are the saddle-node bifurcation, and the existence of a “global reinjection” mechanism that takes the trajectory (once it has passed the threshold) through a large excursion in phase space and returns it to the stable fixed point. These ingredients also exist for the ghostburster near the bifurcation from periodic firing to bursting. There is a saddle-node bifurcation (of periodic orbits) and a global reinjection mechanism in the form of the decrease of  $p_d$  during a burst and then its rapid increase between bursts. Thus there should be excitable behaviour near the bifurcation from periodic firing to bursting, but with the quiescent fixed point and action potential (for normal excitability) replaced by periodic firing and a burst, respectively<sup>26</sup>.

This type of burst excitability is shown in Fig. 9. Here,  $I$  was stepped from 8.3 to either 10.5 (thin line) or 11 (bold line) during the interval  $300 < t < 310$ . (Note that for  $I = 8.3$ , the system is firing periodically.) The smaller step failed to induce a burst (i.e. did not push the system past threshold) and the system returned directly to its previous state, namely periodic firing. The slightly larger step did induce a burst, as seen from the slow decrease and then rapid increase in  $p_d$ . Note that most of the burst occurred after  $I$  had returned to its original value, another signature of the excitable nature of the system.

This type of burst excitability was also shown to occur in the minimal model<sup>27</sup> (9)-(10) and Laing *et al.*<sup>26</sup> showed that it occurred in the more realistic multi-compartmental model<sup>8</sup>. These authors also discussed the possible relevance of burst excitability to communication between weakly electric fish, and derived a scaling relationship between the size and duration of a stimulus that is needed to produce a burst in the ghostburster (or any other similar excitable system). Several authors have proposed that bursts rather than action potentials could be the fundamental units of neural communication<sup>31,32</sup>, and the ghostburster is an example of a neuron which robustly produces bursts in response to physiologically-realistic perturbations in input.

#### 5.4. Differential Modulation of Burst Discharge

The multi-compartmental model<sup>8</sup> and a modification of the minimal model presented in Sec. 5.1 were used by Noonan *et al.*<sup>13</sup> to reproduce and under-

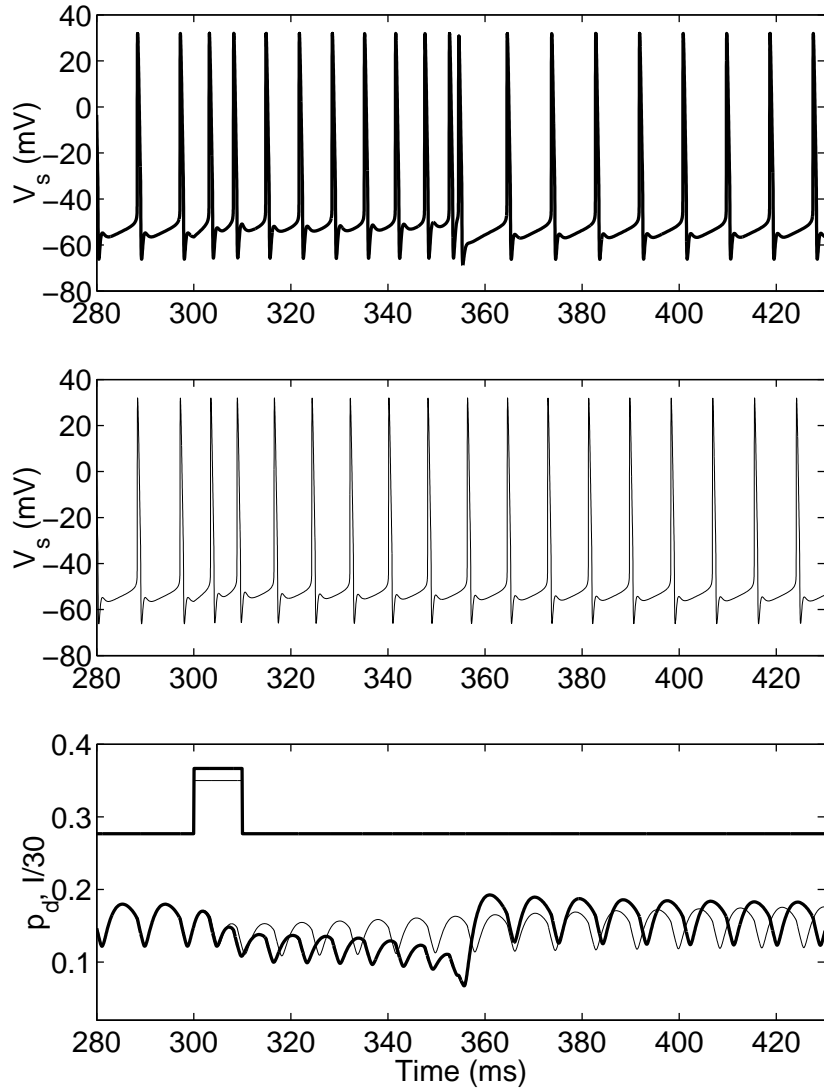


Fig. 9. Burst excitability in (1)-(6). Two different current pulses (shown in bottom panel, 1/30 their actual size) were applied. The larger one (bold) induced a burst (top panel, where the somatic voltage is plotted), while the smaller one (thin line) did not (middle panel, showing somatic voltage). Top and middle panels:  $V_s$  as a function of time. Bottom panel:  $p_d$  and  $I/30$ . See text for more detail.

stand the different effects that somatic and dendritic potassium channels have on burst length. As explained above, the different widths of the somatic and dendritic action potentials (APs), and the slow increase in the width of the dendritic APs during a burst, are an essential part of the bursting mechanism. In both the soma and the dendrite, the flow of potassium ions is responsible for the repolarization of APs. By blocking potassium channels in the neuron's dendrite, dendritic APs become wider, enhancing the size of the DAPs that appear at the soma. This causes bursts to become shorter (if the neuron is already bursting) or can cause the neuron to start bursting (if it is below, but near, the periodic/burst bifurcation).

Conversely, if potassium channels at the soma are blocked, somatic APs become wider, thus lessening the size of the DAPs. This causes bursts to become longer (if the neuron is already bursting) or stop altogether, leaving the neuron firing periodically. The advantage of using such a simple model as (9)-(10) to study an effect like this is that the behaviour of interest could be seen by simply following a curve of saddle-node bifurcations of fixed points in the parameter plane<sup>13</sup>.

## 6. Parallel Processing with Bursts and Isolated Spikes

The original experimental characterization of ELL pyramidal cell burst discharge was in response to static depolarizing inputs<sup>3,6,9</sup>. As described above, there have been successful theoretical efforts in characterising the response of the ghostbuster system to periodic inputs as well as to instantaneous step depolarizations. However, weakly electric fish thrive in a sensory environment with very rich temporal structure. Prey inputs and natural scenes, such as the electric image of the fish's own tail, are typically composed of only low frequency components (0-10 Hz). This is in contrast to intra-specific communication calls that are broadband in their spectral content (0-200 Hz). An often-used simplification of natural scenes is to model its temporal structure as Gaussian band-limited noise. It should be mentioned that this simplification is not always appropriate, most notably in the auditory system<sup>33</sup>. Nevertheless, this strategy has been successfully employed on numerous occasions in *in vivo* electric fish studies<sup>10,34,35</sup>. A study of how the *in vitro* ghostbuster system processes stochastic inputs has only recently been undertaken<sup>36,37,38</sup>. This section will briefly describe the main findings of these studies.

### 6.1. *Ghostbusting the Ghostburster*

In Oswald *et al.*<sup>36</sup> broadband Gaussian stimuli (0–60 Hz) were applied to ELL pyramidal cells in a slice preparation. The spike trains observed were quite distinct from those observed in response to static depolarizations. Notably, the random stimuli elicited a mixture of both isolated spike discharge and bursting, with bursts often consisting of only two spikes and without the characteristic large AHP at burst termination. The difference between autonomous and driven burst discharges is presumably that the high-frequency components in the stimulus — specifically, rapid hyperpolarizations — prematurely terminate burst discharges before a full burst is completed. This assumption can be used to greatly simplify the mathematical modelling of the burst mechanism.

The ghostbursting mechanism described in Sec. 2 involves three main components: 1) a dendritic dependent DAP at the soma, 2) a potentiation of the DAP over a burst event, and 3) a longer refractory period of the dendritic action potential as compared to the somatic action potential. The relatively slow timescale of the dendritic potassium inactivation allows for significant DAP potentiation, typically only over bursts of many spikes; this is evident in both Figs. 1 and 2. Somewhat less apparent from the modelling presented in this review is that the dendritic refractory period is not a fixed quantity, but increases as more spikes occur during a burst. This was demonstrated experimentally by Noonan *et al.*<sup>13</sup>. In this paper the authors forced the neuron to discharge periodically with inter-spike intervals between 5 and 7 ms and observed that dendritic spike failures occurred only after multiple (approximately 5) dendritic spikes, indicating that earlier spikes acted to dynamically increase the dendritic refractory period.

The lack of many-spike bursts in response to broadband Gaussian stimuli permits an approximation of ELL burst dynamics that contains only DAPs and ignores burst mechanism components 2) and 3). Motivated by past leaky integrate-and-fire modelling of ghostbursting<sup>13,27</sup> the following description was postulated<sup>37,38</sup>

$$\frac{dV}{dt} = -V + \gamma x(t - \sigma) + I_{stim}(t) \quad (13)$$

$$\frac{dx}{dt} = y \quad (14)$$

$$\frac{dy}{dt} = -\alpha^2 x - 2\alpha y + \alpha^2 \sum_n \delta(t - t_n) \quad (15)$$

with the rule that once  $V$  reaches 1 from below,  $V$  is reset to 0 and held there for a time  $\tau_r$  before being allowed to continue evolving under (13). Time is measured in units of the membrane time constant. The firing times,  $\{t_n\}$ , are defined to be the times at which  $V$  reaches 1.

The dynamics of (13)-(15) is quite simple in comparison to those of the full conductance-based ghostbursting system (1)-(6) or even those of the reduced model (9)-(10). Equation (13) is a standard leaky integrate-and-fire description of spiking dynamics with a refractory period  $\tau_r$ . The solution of the subsystem  $(x, y)$  with the initial conditions  $x(0) = 0$  and  $y(0) = \alpha^2$  is the so-called alpha function:  $x(t) = \alpha^2 t e^{-\alpha t}$ . Every time  $V(t)$  spikes, there is a time delay  $\sigma$ , after which an alpha function of intensity  $\gamma$  drives the membrane dynamics; this models the dendritic DAP's influence on somatic spike generation. In contrast with (9)-(10), the DAP dynamics are linear without the possibility of potentiation or refractory dynamics. When  $I_{stim}(t) = I$ , independent of time, the system (13)-(15) gives simple tonic discharge for all values of  $I$ . Thus (13)-(15) is not an autonomous burster, unlike many of the models reviewed in this book. There is no saddle-node bifurcation of limit cycles or chaos for any value of  $I$ . We have thus removed (or “busted”) the “ghosting” behaviour so crucial for our understanding of burst response to static inputs. However, when  $I_{stim}(t)$  is a stochastic process with Gaussian spectra between 0-60 Hz, the dynamics of (13)-(15) reproduces the experimentally-measured first and second order statistics of both the spike train and ISI sequence, as well as the linear signal processing of a broadband input stimulus.

Figure 10A shows numerical simulations of (13)-(15) when driven with broadband Gaussian input. Note the presence of both isolated spikes and bursts of two spikes. Both the dendritic DAP,  $x(t)$ , and the stimulus,  $I_{stim}(t)$ , are also shown. Figure 10B shows bimodal inter-spike interval (ISI) histograms of pyramidal cell spike train data. The model shows similar behaviour with active dendrites ( $\gamma > 0$ ) but unimodal ISI histograms when the dendrite is passive ( $\gamma = 0$ ). To measure action potential patterning we

compute the spike train autocorrelation<sup>39</sup> defined as

$$A(\tau) = \frac{\langle s(t)s(t+\tau) \rangle}{\langle s(t)^2 \rangle}. \quad (16)$$

where  $s(t) = \sum_n \delta(t - t_n)$  and  $\langle \cdot \rangle$  is an average over time.  $A(\tau)$  is the mean corrected probability of observing a spike  $\tau$  time units after (or  $-\tau$  time units before) another spike. “Mean corrected” implies that when  $A(\tau) = 0$  the statistics of  $s(t)$  should be interpreted as having the equivalent statistical structure as a simple Poisson process with the same firing rate.

$A(\tau)$  is shown for both the model and the data in Fig. 10C. After an interval of reduced probability of spiking again, due to refractoriness, there is an interval of enhanced probability of firing a spike at approximately 5–7ms after the previous spike. The probability of firing again then decays rapidly back to Poisson statistics within 10ms of the previous spike. The passive dendrite model ( $\gamma = 0$ ) shows that this increased probability is due to the DAP current promoting spike discharge after a spike, but only for a short period. The combination of both the bimodal ISI distributions as well as the distinct non-Poissonian spike statistics as observed from  $A(\tau)$  allow us to describe the stochastic behaviour of (13)–(15) as bursting. Similar statistics were used to characterize the burst discharge of *in vivo* ELL pyramidal cells<sup>40</sup>.

## 6.2. Spike Train Processing

To investigate the processing done by pyramidal cells, we introduce the coherence  $C(f)$  between the input stimulus  $S$  and the spike train response  $R$ :

$$C(f) = \frac{P_{SR}(f)^2}{P_{SS}(f)P_{RR}(f)}. \quad (17)$$

$P_{SR}(f)$  is the cross spectrum between  $S$  and  $R$ ,  $P_{SS}(f)$  is the power spectrum of  $S$  and  $P_{RR}(f)$  is the power spectrum of  $R$ . Quite simply,  $C(f)$  is the frequency-dependent linear correlation between  $S$  and  $R$ ; it is a number between 0 and 1 with 0 representing no correlation and 1 representing perfect correlation at a given frequency  $f$ . The coherence between the full spike train and the stimulus for both the data and the model system (13)–(15) is relatively broadband (slightly lowpass), as shown in Fig 11B. This is similar to *in vivo* results when the stimulus is applied to a small fraction of the total receptive field<sup>34</sup>.

In order to better understand pyramidal cell coding, Oswald *et al.*<sup>36</sup> partitioned the full spike train into two component trains: an isolated-spikes

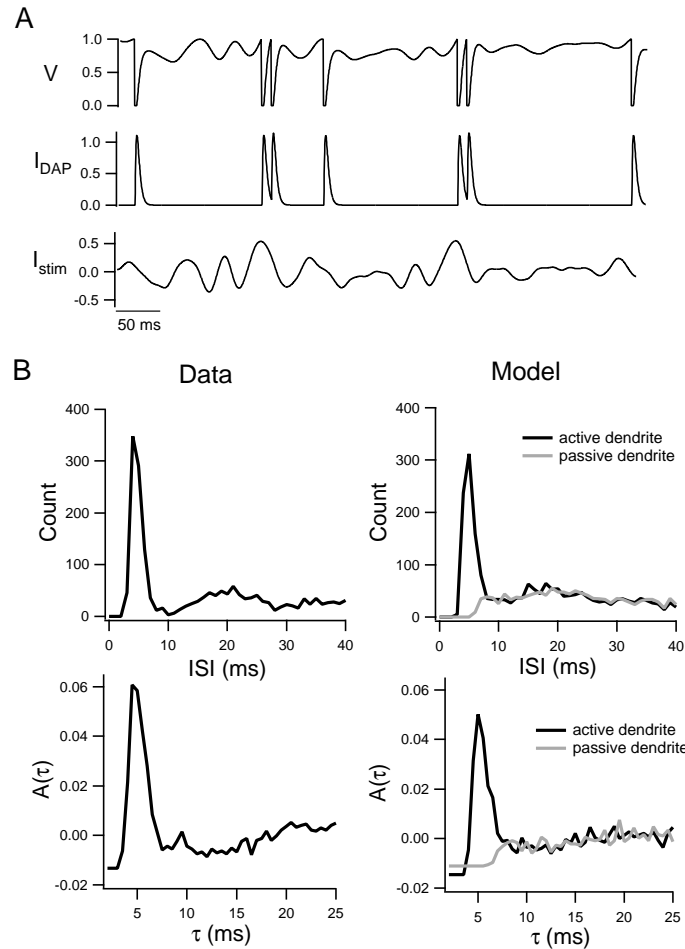


Fig. 10. Stochastic burst discharge in electrosensory pyramidal cells. **A** Time series of  $V(t)$  (top) and  $x(t)$  (middle) when driven with  $I_{stim}$  (shown in the bottom panel). Note the lack of refractory period in the dendritic response  $x(t)$ . **B** ISI histograms (top) and spike train autocorrelation (bottom) for both slice experiment data and the model (13)-(15), computed from 100 seconds of spiking activity. The model results show simulations when the dendrite is active ( $\gamma = 1.2$ ), and when the dendrite is passive ( $\gamma = 0$ ). Other model parameters are  $\sigma = 0.2$ ,  $\tau_r = 0.2$ ,  $\alpha = 12.5$ ,  $\langle I_{stim} \rangle = 0.88$ , and  $\sqrt{\langle I_{stim}^2 \rangle - \langle I_{stim} \rangle^2} = 0.185$ . The membrane time constant was taken to be 5 ms. The experimental methodology is as described in Oswald *et al.*<sup>36</sup>. Data provided by Anne-Marie Oswald.

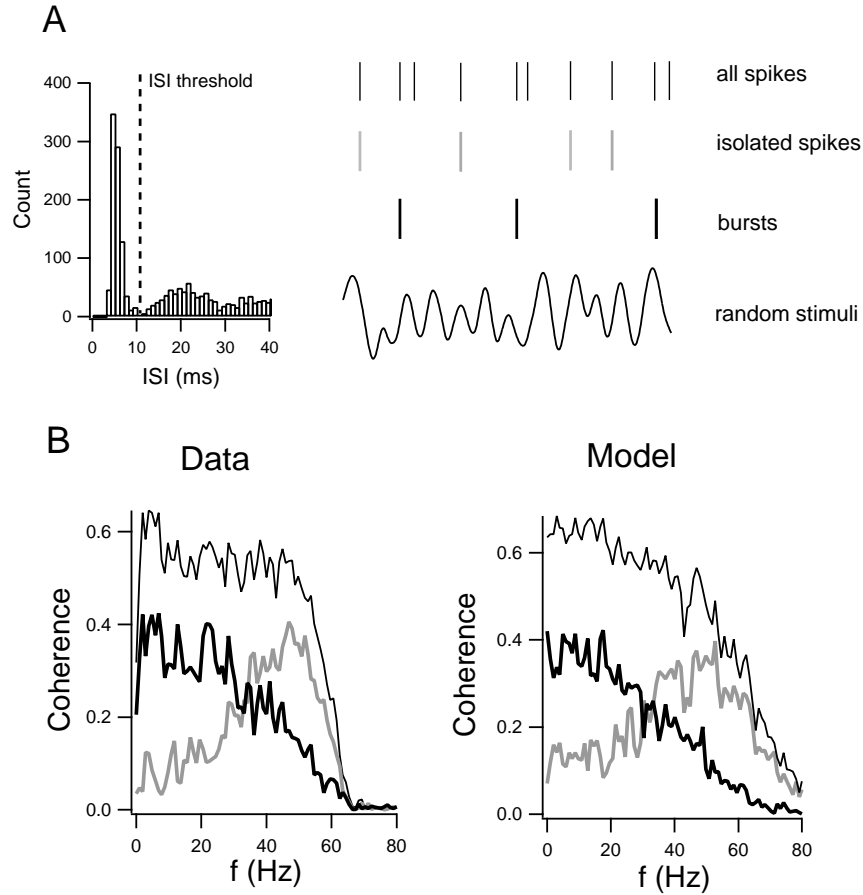


Fig. 11. Parallel processing of dynamic stimuli by bursts and isolated spikes. **A** An ISI threshold of 10ms is used to partition the spike train into isolated spikes (for which both neighbouring ISIs are greater than 10ms) and bursts (spikes for which an ISI is less than 10ms). The time at which a burst occurs is taken to be the time at which the first spike in the burst occurs. **B** The coherence between the full spike train (thin black line), isolated spike train (gray line) and burst train (thick black line), and the stimulus (Gaussian noise with power between 0-60 Hz). The details for both the data and the model are identical to those for Fig. 10. Data provided by Anne-Marie Oswald.

train and a burst train. This partitioning is schematically shown in Fig. 11A and briefly described here. Every spike in a spike train defines two ISIs: the ISI that it begins and the one that it terminates. An ISI threshold corresponding to the local minimum of the ISI probability distribution is

set. If both ISIs that a given spike defines are greater than this threshold, then that spike is considered an isolated spike. In a complementary sense, if one or both of the ISIs are less than the threshold then that spike is involved in a burst. The burst train is further simplified by removing all but the first spike in a burst; the results presented are not sensitive to this reduction.

Interestingly, the coherence between the burst train and the stimulus is low-pass while the coherence between the isolated-spikes train and the stimulus is high-pass (sometimes band-pass). This occurs in a statistically-significant fashion in experiments, in the reduced model (13)-(15), and in a modified version of the full ghostbuster system (1)-(6). (See Fig. 11B and Oswald *et al.*<sup>36</sup> for results not shown.) Thus, this separation of the spike train reveals the potential for the pyramidal cell to selectively code for both low-frequency components via bursts and high-frequency components via isolated spikes. Furthermore, this coding occurs in parallel since the full spike train simultaneously carries both bursts and isolated spikes (providing that the stimulus is dynamic).

The usefulness of this parallel coding by bursts and isolated spikes of a broadband signal presupposes that the decoding mechanisms of higher brain centers are sensitive to this sort of encoding. ELL pyramidal cell output is decoded in the torus semicircularis (TS) of the midbrain. Fortune and Rose<sup>41</sup> have shown that different TS cells have distinct tuning properties with respect to external *in vivo* inputs: specifically, some show low-pass characteristics while others have a high-pass nature. Oswald *et al.*<sup>36</sup> suggested that their low-/high-pass nature was synaptically mediated to respond selectively to either bursts or isolated spikes from ELL pyramidal cells. However, much more work must be done to decisively conclude this point.

## 7. Summary

We have given an overview of a recently-characterised form of neural bursting, known as “ghostbursting”, that occurs in pyramidal cells of weakly electric fish. We have described the various stages involved in its analysis, from experimental observations and the construction of a multi-compartmental model to the analysis of simple caricatures involving two or three differential equations. In the process of analysis we have found a number of features of ghostbursting that do not appear in any previous bursting models. We have also discussed the possible “use” made of the bursting dynamics by

the electric fish, in terms of the processing of electrosensory signals, and found that these neurons seem to be capable of transmitting at least two parallel streams of information, encoded in the timing of bursts and isolated spikes.

### Acknowledgements

We would like to thank our many ghostbursting collaborators whose ideas have helped to shape the results presented here: André Longtin, Leonard Maler, Ray Turner and students, Anne-Marie Oswald, and Maurice Chacron. We particularly thank Anne-Marie Oswald for providing data for several of the figures and André Longtin for carefully reading the manuscript. B.D. was supported by NSERC (Canada) during the writing of this chapter.

### References

1. W. Heiligenberg. *Neural Nets in Electric Fish*, (MIT Press, Cambridge, MA, 1991).
2. R. W. Turner, L. Maler and M. Burrows, *J. Exp. Biol.* **202**, 1167 (1999).
3. R. W. Turner and L. Maler, *J. Exp. Biol.* **202**, 1255 (1999).
4. R. Krahe and F. Gabbiani, *Nat. Rev. Neurosci.* **5**, 13-23 (2004).
5. M. E. Nelson, Z. Xu and J. R. Payne, *J. Comp. Physiol. A* **181**, 523 (1997).
6. R. W. Turner, L. Maler, T. Deerinck, S. R. Levinson and M. H. Ellisman, *J. Neurosci.* **14**, 6453 (1994).
7. B. Doiron, C. Laing, A. Longtin and L. Maler, *J. Comput. Neurosci.* **12**, 5 (2002).
8. B. Doiron, A. Longtin, R. W. Turner and L. Maler, *J. Neurophysiol.* **86**, 1523 (2001).
9. N. Lemon and R. W. Turner, *J. Neurophysiol.* **84**, 1519 (2000).
10. B. Doiron, M. J. Chacron, L. Maler, A. Longtin and J. Bastian, *Nature* **421**, 539 (2003).
11. B. Doiron, B. Lindner, A. Longtin, L. Maler and J. Bastian, *Phys. Rev. Lett.* **93**, 048101 (2004).
12. B. Doiron, L. Noonan, N. Lemon and R. W. Turner, *J. Neurophysiol.* **89**, 324 (2003).
13. L. Noonan, B. Doiron, C. R. Laing, A. Longtin and R. W. Turner, *J. Neurosci.* **23**, 1524 (2003).
14. X. J. Wang, *Neuroscience* **89**, 347 (1999).
15. R. Aldrich, P. Getting and S. Thomson, *J. Physiol. (Lond)* **291**, 531 (1979).
16. M. Ma and J. Koester, *J. Neurosci.* **15** 6720 (1995).
17. B. Ermentrout, *Neural Comput.* **8**, 979 (1996).
18. J. Rinzel and G. B. Ermentrout, in *Methods in Neuronal Modeling: From*

- Ions to Networks*, Ed. C. Koch and I. Segev, (MIT Press, Cambridge MA, 1998).
19. J. Guckenheimer and P. Holmes. *Nonlinear Oscillations, Dynamical Systems, and Bifurcations of Vector Fields*, (Springer-Verlag, New York, 1983).
  20. E. M. Izhikevich, *Int. J. Bifurcat. Chaos* **10**, 1171 (2000).
  21. J. Keener and J. Sneyd. *Mathematical Physiology*, (Springer-Verlag, New York, 1998).
  22. S. H. Strogatz. *Nonlinear Dynamics and Chaos with Applications to Physics, Biology, Chemistry, and Engineering*. (Addison-Wesley, Reading, MA., 1994).
  23. J. Guckenheimer, K. Hoffman and W. Weckesser, *Int. J. Bifurcat. Chaos* **10**, 2669 (2000).
  24. C. R. Laing and S. Coombes, *Int. J. Bifurcat. Chaos* **15**, (2005).
  25. C. R. Laing, B. Doiron, A. Longtin and L. Maler, *Neurocomputing*, **44-46**, 127 (2002).
  26. C. R. Laing, B. Doiron, A. Longtin, L. Noonan, R. W. Turner and L. Maler, *J. Comput. Neurosci.* **14**, 329 (2003).
  27. C. R. Laing and A. Longtin, *Bull. Math. Biol.* **64**, 829 (2002).
  28. C. R. Laing and A. Longtin, *Phys. Rev. E*, **67**, 051928 (2003).
  29. N. F. Rulkov, *Phys. Rev. Lett.* **86**, 183 (2001).
  30. L. Gammaitoni, P. Hänggi, P. Jung and F. Marchesoni, *Rev. Mod. Phys.* **70**, 223 (1998).
  31. J. E. Lisman, *Trends Neurosci.* **20**, 38 (1997).
  32. E. M. Izhikevich, N. S. Desai, E. C. Walcott and F. C. Hoppensteadt. *Trends Neurosci.* **26**, 161 (2003).
  33. F. Rieke, D. A. Bodnar and W. Bialek, *Proc. R. Soc. Lond. B* **262**, 259 (1995).
  34. M.J. Chacron, B. Doiron, L. Maler, A. Longtin and J. Bastian, *Nature* **423**, 77 (2003).
  35. F. Gabbiani, W. Metzner, R. Wessel and C. Koch, *Nature* **384**, 564 (1996).
  36. A-M. M. Oswald, M.J. Chacron, B. Doiron, J. Bastian and L. Maler, *J. Neurosci* **24**, 4351 (2004).
  37. A-M. M. Oswald, B. Doiron and L. Maler, *submitted* (2004).
  38. B. Doiron. *Electrosensory Dynamics: Dendrites and Delays*. Ph.D. Thesis. University of Ottawa (2004).
  39. F. Gabbiani and C. Koch, in *Methods in Neuronal Modeling: From Ions to Networks*, Ed. C. Koch and I. Segev, (MIT Press, Cambridge, MA, 1998).
  40. J. Bastian and J. Nguyenkim, *J. Neurophysiol.* **85**, 10 (2001).
  41. E. Fortune and G. Rose. *J. Neurosci.* **17**, 3815 (1997).